

Monotonic Testing of 3D Printed SS316L under Multiaxial Loading

KOŘÍNEK M.^{1,a}, HALAMA R.^{1,b}, FOJTÍK F.^{1,c}, PAGÁČ M.^{2,d}, KRČEK J.^{3,e},
ŠEBEK F.^{4,f}, KRZIKALLA D.^{1,a}

¹Department of Applied Mechanics, Faculty of Mechanical Engineering, VŠB – Technical University of Ostrava, 17. listopadu 2172/15, 708 00 Ostrava, Czech Republic

²Department of Machining, Assembly and Engineering Metrology, Faculty of Mechanical Engineering, VŠB – Technical University of Ostrava, 17. listopadu 2172/15, 708 00 Ostrava, Czech Republic

³Department of Mathematics and Descriptive Geometry, Faculty of Mechanical Engineering, VŠB – Technical University of Ostrava, 17. listopadu 2172/15, 708 00 Ostrava, Czech Republic

⁴Institute of Solid Mechanics, Mechatronics and Biomechanics, Faculty of Mechanical Engineering, Brno University of Technology, Technická 2896/2, 616 69 Brno, Czech Republic

^amichal.korinek@vsb.cz, ^bradim.halama@vsb.cz, ^cfrantisek.fojtik@vsb.cz,
^dmarek.pagac@vsb.cz, ^ejiri.krcek@vsb.cz, ^fsebek@fme.vutbr.cz, david.krzikalla@vsb.cz

Keywords: Stainless steel S316L, 3D printing of metal, Multiaxial monotonic loading, Digital Image Correlation Method, Hill yield criterion, isotropic hardening, FEM simulation

Abstract. The aim of this work was to monitor the behaviour of 316L stainless steel produced by 3D printing. The material was tested in the state “as printed”. Digital Image Correlation measurements were used for 4 types of notches. The behaviour of these notches under monotonic loading was investigated in two loading paths – tension and torsion. Based on experimental data, two material models were used in finite element analyses. Subsequently, the load-deformation responses of simulations and experiments were compared. Ductility of 3D printed specimens in “as printed” state is also compared with 3D printed machined samples and samples produced by conventional methods.

Introduction

The austenitic stainless steel AISI 316L is one of the most utilized constructional material for various parts in the power industry and beyond. It is usually used in the conventional wrought state [1] while it has been loaded in tension, torsion, and even combination of both. Nevertheless, it is increasingly utilized in the additively manufactured form [2], as it opens new possibilities. It may be optimized and applied in an organic shape or it can even serve as a custom made part or machine element utilized in the repair or reconstruction of structure, where the commercial products are not available or hardly producible by a conventional manufacturing like the machining. Various process parameters used during the additive manufacturing of 316L have been examined [3, 4]. One of the important outputs are the mechanical properties [5, 6] or porosity [7]. The building direction also plays a vital role [8] and the final surface roughness is of a particular interest [9].

This paper presents new results of the deformation response obtained during monotonic multiaxial loading of the samples made from Stainless Steel 316L (SS316L) produced by

Selective Laser Melting (SLM) technology in “as printed” state. Due to the character of the specimens that contain notches, the Digital Image Correlation Method (DICM) was used. The DICM is a progressive optical-numerical method suitable for 3D analysis of structural components, under uniaxial and multiaxial loading in the full-field [10, 11]. Averaged characteristics gained in this experimental study with DIC measurements were used for validation of a numerical model based on Finite Element Method (FEM).

Experiment description

For the test were used the samples created with SOLIDWORKS 2019 (Dassult Systemes SoliDWorks, France) and made using Powder Bed Fusion 3D printing technology– Selective Laser Melting. The machine used was 3D printer Renishaw AM400 (Renishaw, Great Britain, 2016) and material was atomized SS316L powder. This is additive manufacturing technology, where the laser scans and selectively melts the atomized metal powder particles, bonding them together and building a model layer-by-layer [12, 13]. In the beginning of the process, the build chamber is filled with inert gas argon, to minimize the oxidation of metal powder. The layer thickness was set to 50 μm and Chessboard strategy was used. Strategy translates by 5 mm in horizontal direction X and Y and rotates for optimum homogeneous distribution of stress [14, 15]. Other 3D Printing parameters are shown in Table 1 (QuantAM, SW made by company Renishaw) [16]. Building time was 76 hours. The part orientation and the position in chamber, the 3D printing preview and chessboard strategy preview in cross-section are in the Figure 1.

Table 1: 3D Printing parameters [15, 17]

3D Printer:	Renishaw AM400
Powder description:	SS Powder AISI 316L (DIN 1.4404)
Powder Particle Size:	15–45 μm
Layer Thickness:	50 μm
Focus Size:	70 μm
Print Strategies:	Chessboard
Border Power:	110 W
Border Exposure Time:	100 μs
Border Point Distance:	20 μm
Hatches Power:	200 W
Hatches Exposure Time:	80 μs
Hatches Point Distance:	60 μm
Jump speed:	5000 $\text{mm}\cdot\text{s}^{-1}$
Dosing time:	7 s
Melting range:	1371 $^{\circ}\text{C}$ to 1399 $^{\circ}\text{C}$
Concentration of Oxygen:	< 0,1 % O_2
Inert Gas:	Argon
Purity:	5.0 (99.998 %)

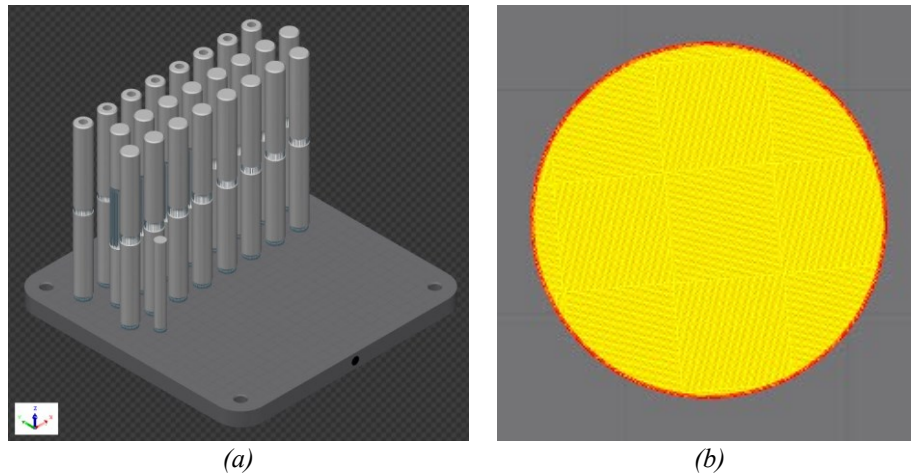


Figure 1: The part orientation and the position in chamber: (a) the 3D printing preview, (b) chessboard strategy preview in cross-section

The specimens were not further machined (outer surface), or heat treated (“as printed”) therefore had naturally a high surface roughness. The geometry of notches considered in this study is shown in Fig. 2. The only one was tubular, other were solid bodies. Tubular (specimens A) had to be drilled on required internal diameter. Each specimen was 160 mm long and outer diameter was 15 mm. In addition, the standard tensile test has been performed. The solid specimens were loaded only in tension. The tubes were subjected to two different loading modes: tension and torsion. Each measurement was repeated four times. Testing machine LabControl 100kN/1000Nm was used. Multiaxial tests were done under deformation control under 2 millimetres per minute for tension and under 0.157 radians per minute for torsion. The results of tests were evaluated in the form of force (torque) vs elongation (twist) diagrams.

DIC measurements were used to monitor the deformation. This method is characterized by the creation of a light area with dark points, also known as pattern. Represented pattern is shown in Fig 3. Two optical sensors were used for this measurement. Sensors are high resolution cameras. The principle of DIC measurement is, that two images of the specimen are compared at different loading state by using a pixel. Advantages of this method are ability to monitor deformation of very complex shaped areas and determination of Young’s modulus and Poisson’s ratio [18]. MERCURY RT system provided by Sobriety company was used for all DIC measurements. This software was also used for configuration and calibration cameras. The optical probe must be set up in this software before starting the measurements. This probe must be aligned for both cameras. The optical probe provides initial length and must cover the whole area examined.

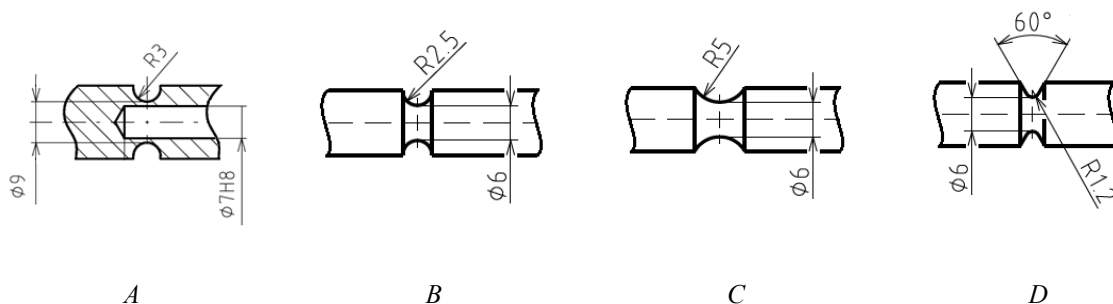


Fig. 2: Notched specimens: The tubular specimen with notch for multiaxial loading (A), and solid specimens with notch for axial loading (B), (C) and (D).



Fig. 3: Representative pattern for DIC measurement

Numerical Modelling

Finite element modelling approach, material models used, and presentation of results are discussed next.

Finite Element Modelling Approach. Since additive manufacturing technology is getting increasingly popular, it is important to examine if FEM approach can predict sufficiently accurate results with respect to experimental response of material. Number of analyses were thus performed in this study to validate finite element model response under several loading conditions. Validation of FEM was performed in terms of comparison of results from FEM with results from experiments.

For purposes of FEM, specimens were modelled as cut-outs of length equal to initial length measured by a probe during experiments. Various levels of symmetry were utilized to reduce computation time. For tensile analyses 1/8 symmetry was used and for torsion analyses half symmetry was used. Models were meshed using linear hexagonal elements (SOLID185). Usage of mapped mesh and sizing settings ensured regular and sufficiently sized mesh to capture stress and strain gradients accurately (example of mesh is in Fig. 4. All analyses were prescribed in form of macros in Ansys Parametric Design Language for easy and fast running and automatic post-processing of desired results.

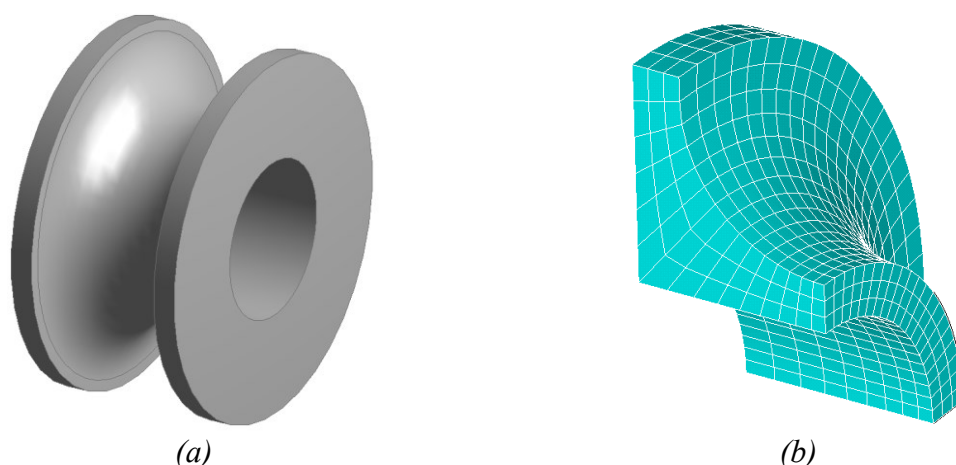


Fig 4.: (a) Model of full specimen A cut-out, and (b) meshed specimen utilizing 1/8 symmetry

Boundary conditions were set in accordance with experimental loading conditions and symmetry assumptions. For simulations of tensile test, nodal displacement and symmetry plane boundary conditions were used. Those were applied upon nodes within appropriate faces. See

Fig. 5a for an example of boundary conditions for tensile test simulations as it is similar for all specimens.

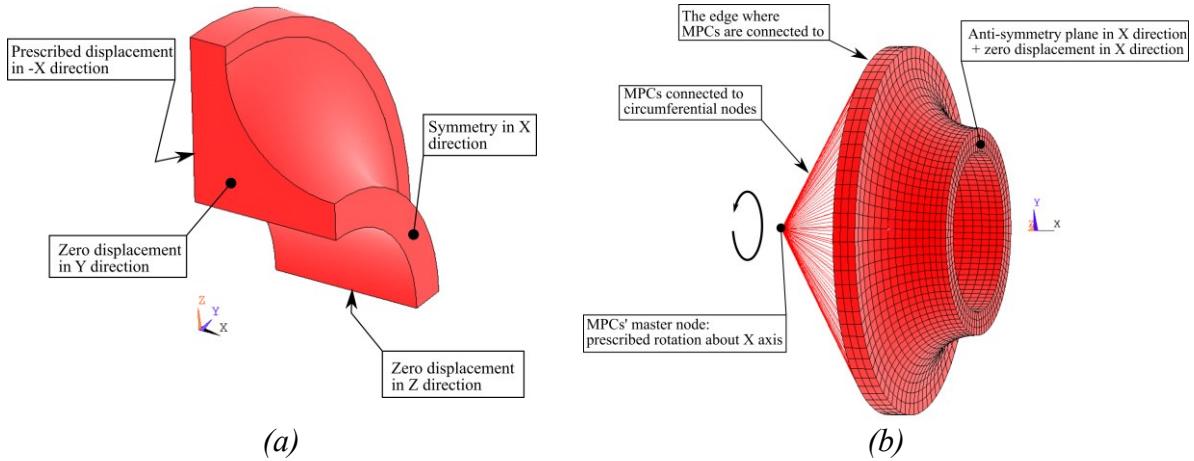


Fig 5: Description of boundary conditions for tensile test simulation (a), and for torsion test simulation (b)

For simulation of torsion test of specimen A, structural multipoint constraints (MPC184) were utilized to load the specimen in torsion. Then nodal displacement in “x” direction and anti-symmetry plane in “x” direction were used (see Fig. 5b). Fix of displacement of nodes in “x” direction was sufficient since Ansys’s anti-symmetry plane formulation constraints - in this case - all other degrees of freedom. Observing boundary conditions, one can see that all simulations were displacement controlled. Correctness of applied boundary conditions for both tensile and torsion test simulations were confirmed by simulations of full models.

Material Model. To simulate the material response of specimens under conditions of tension and torsion, a suitable material model was needed. The chosen material model captures nonlinear isotropic hardening together with either Hill yield criterion or von Mises yield criterion. The linear elastic part of the model obeys Hooke’s law for three-dimensional problem denoted in Table 2 and requires two input parameters of Young’s modulus E and Poisson ratio μ . Values of the parameters are denoted in Table 3.

Table 2: Hooke’s law for three-dimensional problem

$$\varepsilon_x = \frac{1}{E} [\sigma_x - \mu(\sigma_y + \sigma_z)], \varepsilon_y = \frac{1}{E} [\sigma_y - \mu(\sigma_x + \sigma_z)], \varepsilon_z = \frac{1}{E} [\sigma_z - \mu(\sigma_y + \sigma_x)],$$

$$\gamma_{xy} = \frac{\tau_{xy}}{G}, \gamma_{yz} = \frac{\tau_{yz}}{G}, \gamma_{xz} = \frac{\tau_{xz}}{G},$$

where σ_i - stress components, ε_i - normal strain components, γ_{ij} - shear strain components, τ_{ij} – shear stress components and G - shear modulus.

Table 3: Elastic parameters

Parameter	Value	Unit
E	183	[GPa]
μ	0.3	[-]

Isotropic hardening is suitable for this study since the loading was monotonic. Isotropic hardening during plastic deformation causes a uniform increase of the yield surface. This results in increased yield stress. Thus, the yield criterion takes the form:

$$f(\sigma) - Y = 0 \quad (1)$$

where $f(\sigma)$ is function of stress and Y is yield stress (or size of yield surface). For description of isotropic hardening, the Voce law was used. Voce law is, however, combination of linear and nonlinear isotropic variables and has the form:

$$Y = \sigma_Y + R \quad (2)$$

where σ_Y is initial yield stress and R is a new internal variable. The evolution of R is done by superposition of two parts:

$$dR = dR_1 + dR_2, \quad dR_1 = R_0 dp, \quad dR_2 = b(R_\infty - R_2)dp \quad (3)$$

By integration of Eq. (3) with zero initial values of p , R_1 and R_2 respectively and use of Eq. (2), a constitutive equation is obtained:

$$Y = \sigma_Y + R_0 p + R_\infty(1 - e^{-bp}) \quad (4)$$

where R_0 is slope of the saturation stress, p is accumulated equivalent plastic strain, R_∞ is the difference between the saturation stress and the initial yield stress and b is hardening parameter that governs the rate of saturation of the exponential term. Values of the parameters are denoted in Table 4.

Table 4: Voce law parameters

Parameter	Value	Unit
σ_Y	575	[MPa]
R_0	950	[MPa]
R_∞	60	[MPa]
b	125	[-]

Hill yield criterion and von Mises criterion were used in this material model to compare their accuracy with respect to real additive manufactured specimens' responses. Hill criterion is anisotropic, independent of hydrostatic pressure and depends on the orientation of the stress relative to the axis of anisotropy, thus suitable for materials in which microstructure influences the macroscopic behaviour of the material, what is the case for additive manufactured steels [19, 20]. Hill yield criterion was, in this study, utilized for modelling of yield strength anisotropy based on build direction [21 - 24]. Hill yield criterion's stress function has the form:

$$f(\sigma) \equiv F(\sigma_{22} - \sigma_{33})^2 + G(\sigma_{33} - \sigma_{11})^2 + H(\sigma_{11} - \sigma_{22})^2 + 2L\sigma_{23}^2 + 2M\sigma_{31}^2 + 2N\sigma_{12}^2 = \sigma_y^2 \quad (5)$$

where F , G , H , L , M , N are coefficients which are functions of the ratio of the scalar yield stress parameter and yield stress in each of the six stress components. The coefficients and ratios are denoted in Table 5 [25 - 27].

Table 5: Hill yield criterion coefficients and ratios

$$\begin{aligned}
 F &= \frac{1}{2} \left(\frac{1}{R_{22}^2} + \frac{1}{R_{33}^2} - \frac{1}{R_{11}^2} \right), G = \frac{1}{2} \left(\frac{1}{R_{33}^2} + \frac{1}{R_{11}^2} - \frac{1}{R_{22}^2} \right), H = \frac{1}{2} \left(\frac{1}{R_{11}^2} + \frac{1}{R_{22}^2} - \frac{1}{R_{33}^2} \right), \\
 L &= \frac{3}{2} \left(\frac{1}{R_{23}^2} \right), M = \frac{3}{2} \left(\frac{1}{R_{13}^2} \right), N = \frac{3}{2} \left(\frac{1}{R_{12}^2} \right), \\
 R_{11} &= \frac{\sigma_{11}^y}{\sigma_y}, R_{22} = \frac{\sigma_{22}^y}{\sigma_y}, R_{33} = \frac{\sigma_{33}^y}{\sigma_y}, \\
 R_{12} &= \sqrt{3} \frac{\sigma_{12}^y}{\sigma_y}, R_{23} = \sqrt{3} \frac{\sigma_{23}^y}{\sigma_y}, R_{13} = \sqrt{3} \frac{\sigma_{13}^y}{\sigma_y},
 \end{aligned}$$

where the directional yield stress ratios R_{ii} and R_{ij} are related to the isotropic yield stress parameter, and σ_i^y is the yield stress in the direction given by the value of subscript i . Almost all directional yield stress ratios for uniaxial and torsional loading are equal to 1. The only different one is the directional ratio R_{33} which is equal to 0.87. The ratio R_{33} corresponds to axial direction of all specimens, thus introduces the effect of build direction into the material model.

Von Mises yield criterion is isotropic, independent of hydrostatic pressure and commonly used for metals, polymers, etc. Independence of hydrostatic pressure can limit its applicability to micro structured materials. In this study, accuracy of the von Mises yield criterion is examined by comparing to the real material response. Von Mises stress function takes the form:

$$f(\boldsymbol{\sigma}) = \sqrt{\frac{(\sigma_{11} - \sigma_{22})^2 + (\sigma_{22} - \sigma_{33})^2 + (\sigma_{11} - \sigma_{33})^2}{2}} \quad (6)$$

where σ_{ii} are principal stresses.

Results

All specimens were subjected to loading as described above. Each test was deformation controlled. Values of applied force or torque were recorded by testing machine and values of deformation were recorded by DICM system. Because experimentally measured data embodies natural oscillations, the presented force vs. elongation diagrams were smoothed using functions of the Curve Fitting Toolbox in Matlab. The combination of moving average and smoothing splines seemed to lead to sufficient results. Optimal smoothing parameters were chosen with respect to the size and character of data sets.

Presentation of simulation results and their comparison with respect to experimental response of specimens follow next. The comparison is performed in form of plots comprised of experimental smoothed responses in dashed lines and simulation results in full lines (see Fig. 7 - 11).

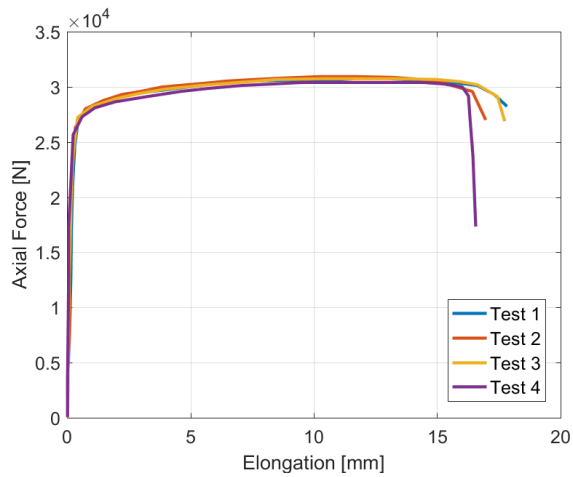
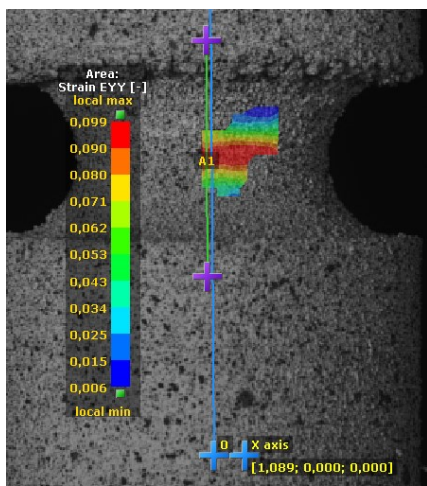
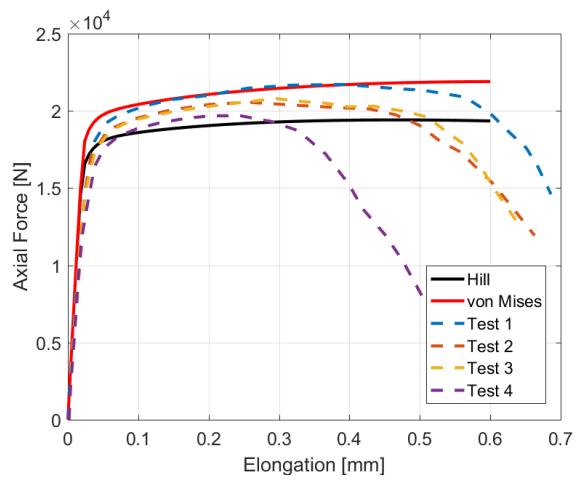


Fig. 6: Dependency of force on elongation for tensile test

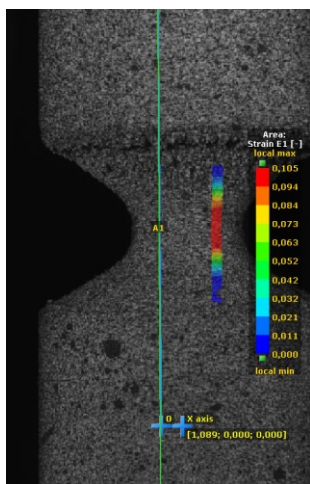


(a)

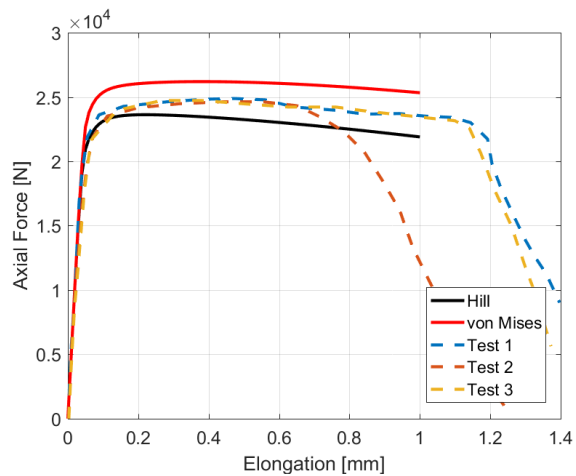


(b)

Fig. 7: Longitudinal strain distribution (a), and dependency of force on elongation for specimen type A compared to experimental and simulation results (b)

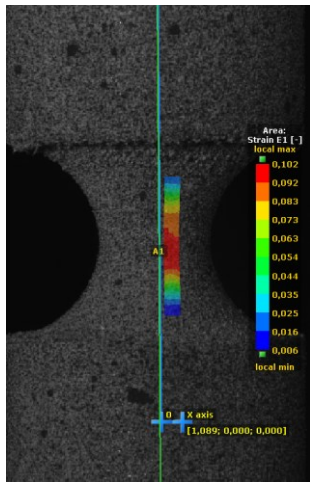


(a)

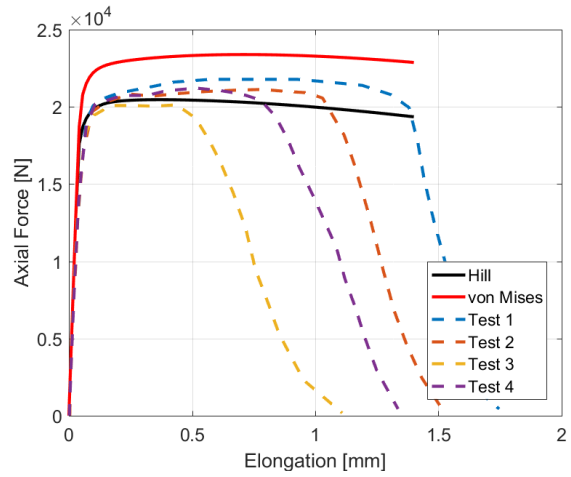


(b)

Fig. 8: Maximal principal strain distribution (a), and dependency of force on elongation for specimen type B compared to experimental and simulation results (b)

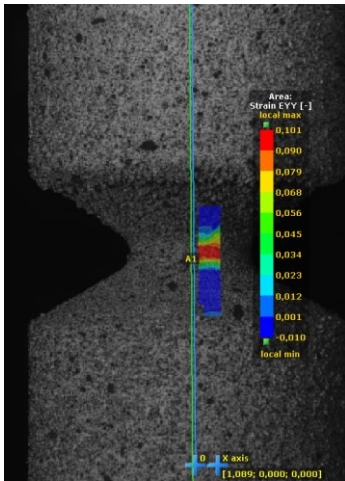


(a)

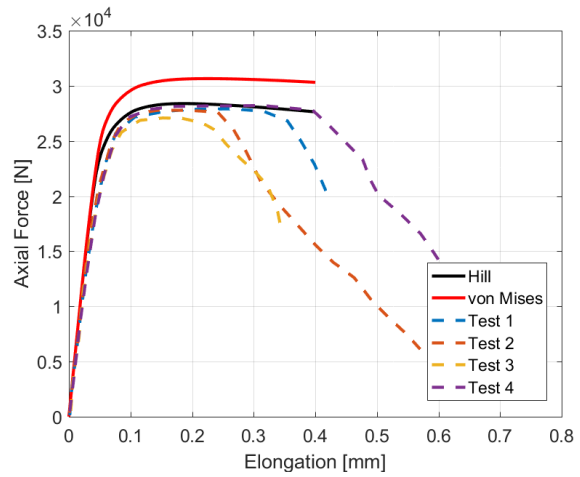


(b)

Fig. 9: Maximal principal strain distribution (a), and dependency of force on elongation for specimen type C compared to experimental and simulation results (b)

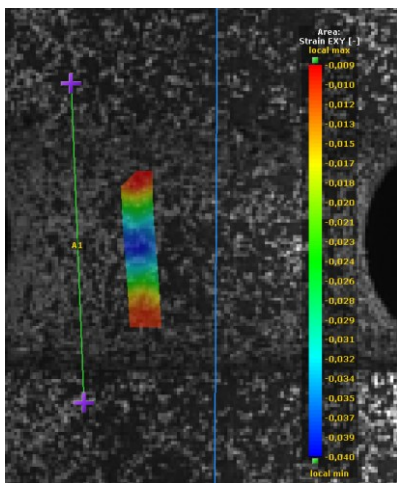


(a)

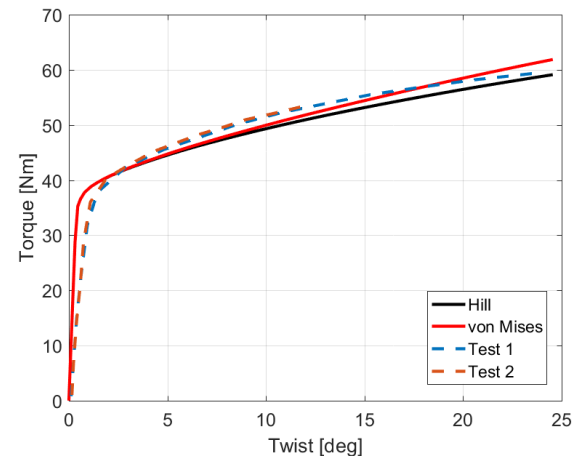


(b)

Fig. 10: Longitudinal strain distribution (a), and dependency of force on elongation for specimen type D compared to experimental and simulation results (b)



(a)



(b)

Fig. 11: Shear strain distribution for torsional test (a), and dependency of torque on twist for specimen type A compared to experimental and simulation results (b)

Comparison of experimental results with results from FEM analysis revealed that simulation based on Hill yield criterion gives more accurate results than simulation based on isotropic yield criterion. Usage of isotropic yield criterion leads to stiffer response of simulation model for each specimen type. Thus, usage of Hill yield criterion could be crucial for obtaining reasonably accurate results from FEM analysis once simulating additive manufactured steels such as SS316L. Depending on directional yield stress ratios (which were, in this study, correlated from experimental material response), the Hill yield criterion can give more compliant response than the real material response is. Such a phenomenon was observed for majority of responses in this study (see Fig. 6 - 11). In this case, one should be aware that once having a displacement-controlled simulation the stresses are likely to be underestimated.

Ductility was calculated from tensile test results for specimen without notch (Fig. 6).

$$A = \frac{L_u - L_0}{L_0} \cdot 100 [\%], \quad (7)$$

where L_u is the final length of the specimen after the test and L_0 is initial length of the specimen. Specimens without machined outer surface had ductility from 42 % to 45 %. "As printed" specimens show about 2/3 higher ductility than machined specimens. The machined samples had ductility 13 % to 15 %. The printed SS316L reveals surprisingly good ductility even printed in vertical direction (43 % in comparison with 60 % of the conventional SS316L), but just for "as printed" variant.

Conclusions

Objective of this paper was also to study the effect of machining. Four types of specimen were investigated. The geometry of the specimens is show in Fig 2. In addition, the standard tensile test has been performed. The specimens were subjected to different loading modes, as stated above. All specimens were made from Stainless Steel 316L produced by Selective Laser Melting Technology in "as printed" state. DICM was used to monitor deformation. DIC method is a good alternative for complicated shape areas such as notches. Averaged characteristics gained in this experimental study were used for validation of a numerical model based on FEM.

Acknowledgement:

This work was supported by The Ministry of Education, Youth and Sports from the Specific Research Project (SP2020/23), by the Czech Science Foundation (GACR), grant No. 19-03282S and has been done in connection with the DMS project reg. no. CZ.02.1.01/0.0/17_049/0008407 financed by Structural Funds of Europe Union.

References

- [1] F. Šebek, P. Kubík, J. Hůlka, J. Petruška, Strain hardening exponent role in phenomenological ductile fracture criteria, *Eur. J. Mech. Solids A* 57 (2016) 149–164.
- [2] M. Marya, V. Singh, S. Marya, J.Y. Hascoet, Microstructural development and technical challenges in laser additive manufacturing: Case study with a 316L industrial part, *Metall. Mater. Trans. B* 46 (4) (2015) 1654–1665.
- [3] J. Metelkova, Y. Kinds, K. Kempen, Ch. de Formanoir, A. Witvrouw, B.V. Hooreweder, On the influence of laser defocusing in selective laser melting of 316L, *Addit. Manuf.* 23 (2018) 161–169.
- [4] G. Tapia, S. Khairallah, M. Matthews, W.E. King, A. Elwany, Gaussian process-based surrogate modeling framework for process planning in laser powder-bed fusion additive

- manufacturing of 316L stainless steel, *Int. J. Adv. Manuf. Technol.* 94 (2018) 3591–3603.
- [5] M.S. Pham, B. Dovggy, P.A. Hooper, Twinning induced plasticity in austenitic stainless steel 316L made by additive manufacturing, *Mater. Sci. Eng. A* 704 (2017) 102–111.
- [6] X. Chen, J. Li, X. Cheng, B. He, H. Wang, Z. Huang, Microstructure and mechanical properties of the austenitic stainless steel 316L fabricated by gas metal arc additive manufacturing, *Mater. Sci. Eng. A* 703 (2017) 567–577.
- [7] Z.'E.E. Tana, J.H.L. Pang, J. Kaminski, H. Pepin, Characterisation of porosity, density, and microstructure of directed energy deposited stainless steel AISI 316L, *Addit. Manuf.* 25 (2019) 286–296.
- [8] A. Leicht, U. Klement, E. Hryha, Effect of build geometry on the microstructural development of 316L parts produced by additive manufacturing, *Mater. Charact.* 143 (2018) 137–143.
- [9] Y. Kaynak, O. Kitay, The effect of post-processing operations on surface characteristics of 316L stainless steel produced by selective laser melting, *Addit. Manuf.* 26 (2019) 84–93.
- [10] F. Trebuňa, R. Huňady, M. Hagara. Experimentálne metódy mechaniky - Digitálna obrazová korelácia. Košice: Technická univerzita v Košiciach, 2016. ISBN 978-80-5532-346-6.
- [11] Z. Paška, R. Halama, F. Fojtík, P. Gajdoš, Strain response determination in notched specimens under multiaxial cyclic loading by DICM. In: *Proceedings of EAN 2017 - 55th Conference on Experimental Stress Analysis 2017*, Novy Smokovec, Slovakia, May 30 - 1 June, 2017, p. 143-149.
- [12] I. Gibson, D. Rosen, B. S. Tucker, *Additive manufacturing technologies: rapid prototyping to direct digital manufacturing*. New York: Springer, c2010, xxii, 459 p. ISBN 1441911200.
- [13] 3D Hubs. 2020. Introduction To Metal 3D Printing | 3D Hubs. [online] Available at: <<https://www.3dhubs.com/knowledge-base/introduction-metal-3d-printing/>> [Accessed 16 June 2020].
- [14] J. Hajnyš, M. Pagáč, J. Mesicek, J. Petrů, M. Krol, Influence of scanning strategies parameters on residual stress in SLM process according to bridge curvature method for stainless steel AISI 316L. *Materials*. 2020, 13, 1527. doi: 10.3390/ma13071659.
- [15] J. Hajnyš, M. Pagáč, O. Kotera, J. Petrů, S. Scholz, Influence of Basic Process Parameters on Mechanical and Internal Properties of 316L Steel in SLM Process for Renishaw AM400. *MM Science Journal*, 2019. Pgs: 2790-2794. DOI: 10.17973/MMSJ.2019_03_2018127
- [16] RENISHAW, *Magics training: Material profile editing*. RENISHAW: apply innovation. United Kingdom: Renishaw, 2016. Available from: <https://www.renishaw.com>. [Accessed 16 June 2020].
- [17] Data sheets - Additive manufacturing. Object moved [online]. Copyright © [cit. 16.06.2020]. Available at: <https://www.renishaw.com/en/data-sheets-additive-manufacturing--17862>. [Accessed 16 June 2020]
- [18] D. Lecompte et al., „Quality assessment of speckle patterns for digital image correlation“, *Opt. Lasers Eng.*, roč. 44, č. 11, s. 1132–1145, 2006, DOI: 10.1016/j.optlaseng.2005.10.004.
- [19] L. Hitzler, J. Hirsch, B. Heine, M. Merkel, W. Hall, A. Öchsner, 2017. On the anisotropic mechanical properties of selective laser-melted stainless steel. *Materials*, 10(10), p.1136. DOI: 10.3390/ma10101136
- [20] P. Bian, J. Shi, Y. Liu, Y. Xie, Influence of laser power and scanning strategy on residual stress distribution in additively manufactured 316L steel, *Optics & Laser Technology*, Volume 132, 2020,106477, ISSN 0030-3992, DOI: 10.1016/j.optlastec.2020.106477.

- [21] N. Zhang, H. Li, X. Zhang, D. Hardacre, 2016. Review of the fatigue performance of stainless steel 316L parts manufactured by selective laser melting. Available from: <https://hdl.handle.net/10356/84380>
- [22] S. Afkhami, M. Dabiri, S. H. Alavi, T. Björk, A. Salminen, 2019. Fatigue characteristics of steels manufactured by selective laser melting. *International Journal of Fatigue*, 122, pp.72-83. DOI: 10.1016/j.ijfatigue.2018.12.029
- [23] X. Song, S. Feih, W. Zhai, C. N. Sun, F. Li, R. Maiti, J. Wei, Y. Yang, V. Oancea, L. R. Brandt, A. M. Korsunsky, 2020. Advances in additive manufacturing process simulation: Residual stresses and distortion predictions in complex metallic components. *Materials & Design*, p.108779. DOI: 10.1016/j.matdes.2020.108779
- [24] P. Ferro, F. Berto, L. Romanin, 2020. Understanding powder bed fusion additive manufacturing phenomena via numerical simulation. *Frattura ed Integrità Strutturale*, 14(53), pp.252-284. DOI: 10.3221/IGF-ESIS.53.21
- [25] R. B. Colby, 2013. Equivalent plastic strain for the Hill's yield criterion under general three-dimensional loading (Doctoral dissertation, Massachusetts Institute of Technology).
- [26] T. Altan, A. E. Tekkaya, eds., 2012. *Sheet metal forming: fundamentals*. Asm International.
- [27] M. Bertin, F. Hild, S. Roux, 2017. On the identifiability of Hill-1948 plasticity model with a single biaxial test on very thin sheet. *Strain*, 53(5), p.e12233. DOI: 10.1111/str.12233